

## Research Article

# Flörkeite, $(K_3Ca_2Na)[Al_8Si_8O_{32}]\cdot 12H_2O$ : A Rare Zeolite from Pyrometamorphic Rocks of the Hatrurim Complex, Israel

Katarzyna Skrzyńska<sup>1</sup>, Georgia Cametti<sup>2</sup>, Irina O. Galuskina<sup>1</sup>, Yevgeny Vapnik<sup>3</sup>, and Evgeny Galuskin<sup>1</sup>

<sup>1</sup>University of Silesia, Faculty of Natural Sciences, Institute of Earth Sciences, Sosnowiec 41-200, Poland

<sup>2</sup>University of Bern, Institute of Geological Science, Bern 3012, Switzerland

<sup>3</sup>Ben-Gurion University of the Negev, Department of Geological and Environmental Sciences, Beer Sheva 84105, Israel

Correspondence should be addressed to Katarzyna Skrzyńska; [katarzyna.k.nowak@us.edu.pl](mailto:katarzyna.k.nowak@us.edu.pl)

Received 3 August 2022; Revised 2 October 2022; Accepted 11 October 2022; Published 2 November 2022

Academic Editor: Francis McCubbin

Copyright © 2022 Katarzyna Skrzyńska et al. Exclusive Licensee GeoScienceWorld. Distributed under a Creative Commons Attribution License (CC BY 4.0).

Flörkeite, a rare zeolite with **PHI** (phillipsite) framework type, was found in numerous amygdaloidal voids in pyrometamorphic rocks of the Hatrurim Basin, Hatrurim Complex, Israel. This is the second reported occurrence of flörkeite previously found in a Ca-rich xenolith from a quarry at the Bellerberg volcano near Ettringen, East Eifel volcanic area, Germany. The mineral with the empirical crystal chemical formula  $(K_{2.91}Ca_{2.00}Na_{0.91})[Al_{7.96}Si_{8.04}O_{31.94}]\cdot 12H_2O$  (*P*-1, no. 2,  $a = 19.9366$  (2),  $b = 14.2517$  (1),  $c = 8.89350$  (10) Å,  $\alpha = 88.2480$  (1),  $\beta = 125.0960$  (10),  $\gamma = 89.6350$  (10),  $V = 2019.19$  (4) Å<sup>3</sup>, and  $R = 3.41\%$ ) did not show significant differences with respect to that of the type locality. The Raman spectrum of flörkeite is here reported for the first time. No significant differences are noticed compared to phillipsite-K. The main band  $\sim 470\text{ cm}^{-1}$ , characteristic of the **PHI**-type structures, is independent on framework order and Si/Al ratio. The zeolite mineralization of amygdules in pyrometamorphic rocks results from meteoric water circulations in Al-rich rocks during their cooling. The crystallization sequence of zeolite corresponds to the Ca/(K+Na) ratio decrease. Flörkeite formed at the end of a low-temperature crystallization sequence, indicating the predominant role of potassium in crystallization. The occurrence of flörkeite in different pyrometamorphic rocks implies the relatively uniform, regional mineral-forming conditions, and open hydrologic system of zeolitization. In pyrometamorphic rocks of the Hatrurim Basin, the process of zeolitization is characterized by low silica activity and high pH conditions.

## 1. Introduction

Zeolites occur in diverse geological environments. Generally, their origin can be sedimentary or hydrothermal [1–4]. It is widely known that most zeolites are formed from low-temperature alterations due to water penetrating into rocks. Minerals belonging to the phillipsite (-K, -Na, and -Ca) series are one of the most widespread zeolites. The most frequent is phillipsite-K, which is present in volcanic rocks and in diagenetically altered sediments and deep-sea sediments [5, 6]. The chemical composition of the phillipsite-type minerals depends on the protolith composition. Therefore, they exhibit a wide variation of the extraframework population, reflected in the wide  $R$  ( $R = Si/(Si+Al+Fe^{3+})$ ) range from 0.5 to 0.77 [7]. The zeolite, with **PHI** (phillipsite) framework

type, characterized by the highest aluminum content is flörkeite  $(K_3Ca_2Na)[Al_8Si_8O_{32}]\cdot 12H_2O$ , which stands out because of the completely ordered framework and extraframework sites. Up to now, flörkeite has only been known in a Ca-rich xenolith from a quarry at Bellerberg volcano, East Eifel volcanic area, Germany [8].

Here, we report on the second occurrence of flörkeite, which was found in numerous amygdaloidal voids of the pyrometamorphic rocks from the Hatrurim Basin, Negev desert, Israel. The pyrometamorphic Hatrurim Complex in Israel has been the subject of many mineralogical studies over the last ten years. However, the research has focused chiefly on high-temperature rather than low-temperature minerals. Recent studies have shown the wide zeolites diversity and great potential for the occurrence of rare and new

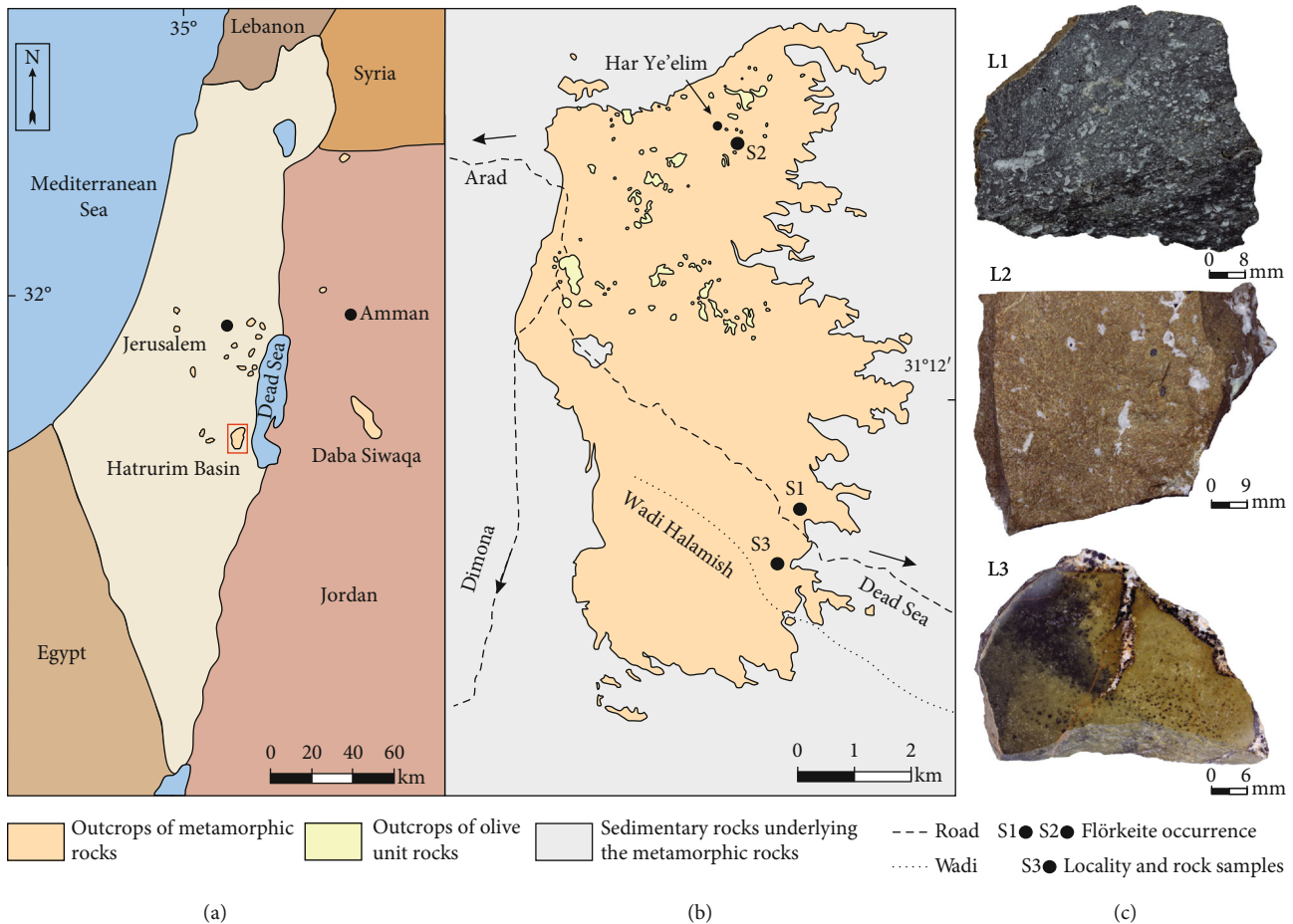


FIGURE 1: (a) Schematic map of the pyrometamorphic rocks outcrops in Israel, Palestinian Autonomy and Jordan; fragment outlined by frame is magnified in (b); (b) Hatrurim Basin outcrops with marked localities of sampling and olive unit outcrops, which is a major unit subjected to zeolitization; (c) rock samples: L1, gehlenite-wollastonite-kalsilite paralava with amygdaloidal texture from Zuk Tamrur; L2, esseneite-latiumite hornfels from Har Ye'elim; L3, gehlenite-wollastonite-garnet hornfels with paralava part from Halamish wadi (modified from Geological Map of Israel 1: 50 000, Arad sheet, [27]).

zeolites [9]. This paper provides data on the chemical composition, structure, and Raman spectroscopy of a rare zeolite—flörkeite—from the rocks of the Hatrurim Complex. Moreover, zeolite genesis is discussed.

## 2. Geological Setting

The Hatrurim Complex, commonly called the Mottled Zone because of its multicolored appearance, is a complex of pyrometamorphic rocks on both sides of the Dead Sea Transform Fault and widespread over the territory of Israel, Palestine Autonomy, and Jordan (Figure 1(a)) [10–13]. It consists of high-temperature rocks and their alteration products. The high-temperature, low-pressure rocks occur as irregular bodies embedded in light-colored, low-temperature calcium-hydrosilicate rocks [9, 14]. The genesis of the Hatrurim Complex is still under debate. Until now, two hypotheses have been suggested. For several decades, the Hatrurim Complex was considered as a result of spontaneous surface combustion [11, 15, 16]. The bituminous chalks and marls of the Ghareb and Taqiye Formations, dated at Maastrichtian to Paleocene age, were subjected to

burning [11, 12]. The second hypothesis relates the origin of pyrometamorphic processes with neotectonics mud volcanism and methane burning [16–18]. The combustion metamorphism event dates to ca. 16 Ma in the Miocene and at 4.0–2.3 Ma in the Pliocene-Pleistocene [12, 19–21]. The temperature of the regional metamorphic processes is estimated at 600–900°C. However, the temperature locally reached up to 1350°C [18]. It led to the protolith's calcination, annealing, or even fusion. As a result, clinker-like mineral associations are formed [11]. The low-temperature hydrothermal stage and supergene processes are linked to the concrete formation (hydrated Portland cement and sulfoaluminate clinkers) [20, 22].

The Hatrurim Basin, a stratotype [23] (Figure 1(b)) of the Hatrurim Complex, stands out among Mottled Zone areas of diverse rock types with high and ultrahigh formation temperatures. It is composed of conical hills separated by wadis [23]. Up to now, there are the following distinguished types of high-temperature rocks: anorthite-pyroxene paralava of the olive unit, spurrite rocks and larnite pseudoconglomerates, fine-grained grey pyrrhotite-bearing amygdaloidal paralava, gehlenite-wollastonite hornfels, coarse-grained

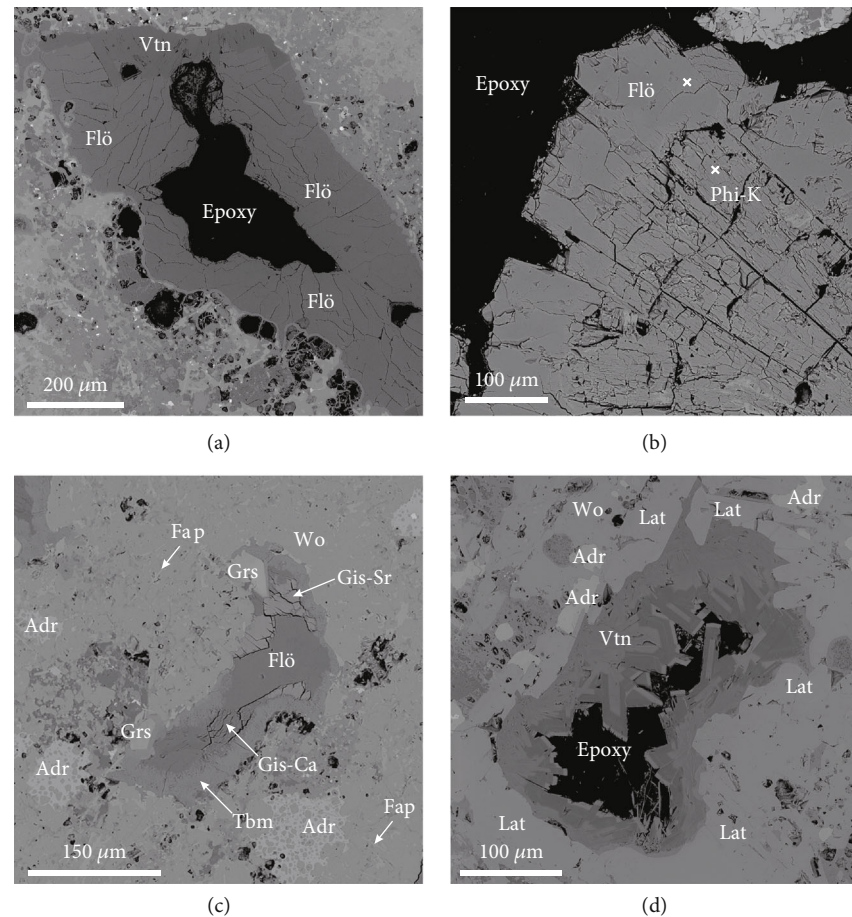


FIGURE 2: BSE images: (a) the void of gehlenite-wollastonite paralava filled with vertumnite and flörkeite; (b) crystals of phillipsite-K overgrown by flörkeite; (c) flörkeite overgrowing gismondine-Sr and gismondine-Ca in amygdale of gehlenite hornfels; x indicates a point of Raman spectra collection; (d) voids of gehlenite hornfels filled by Ba-bearing vertumnite. Adr: andradite; Fap: fluorapatite; Flö: flörkeite; Gis-Ca: gismondine-Ca; Gis-Sr: gismondine-Sr; Grs: grossular; Lat: latiumite; Phi-Ca: phillipsite-Ca; Tbm: tobermorite; Vtn: vertumnite; Wo: wollastonite.

wollastonite-andradite-schorlomite-kalsilite paralava, and recently found fine-grained esseneite-latiumite paralava and hornfels [24]. The high-temperature rocks are surrounded by brecciated metasediments and calcium-hydrosilicate rocks, so-called low-grade Hatrurim. The low-temperature mineralization, which veined pyrometamorphic rocks, is formed due to hydrothermal alteration and weathering processes, especially the interaction of meteoric water and rocks [14, 20, 23, 25]. Additionally, anorthite-pyroxene hornfels of the olive unit, located in the northern part of the Hatrurim Basin, were subjected to zeolitization [9]. Zeolites occur mainly in amygdaloidal voids of pyrometamorphic rocks associated with tobermorite supergroup minerals, minerals of ettringite group, and hydrotalcite supergroup. The veins are mainly filled by carbonates and varying amounts of ettringite and tobermorite group minerals [20, 26], which were formed in the 250–30 Ka range. Thus, they are significantly younger than high-temperature rocks [20]. This age corresponds to intensive weathering in the Southern Levant during interglacial periods [9].

Flörkeite was found in three lithological types of rocks from the 3 localities of the Hatrurim Basin (Figures 1 and 2

and supplementary Figure S1). The samples represent the high-temperature types of pyrometamorphic rocks of the Hatrurim Complex. The first sample (L1, Figure 2(a) and S1a) is composed of gehlenite, wollastonite, kalsilite, fluorapatite, garnet of the grossular-andradite-schorlomite series, chromite, pyrrhotite, and perovskite. In the amygdaloidal voids occur the following minerals: vertumnite, flörkeite, and minerals of the tobermorite supergroup. Flörkeite forms crystals up to 200 µm. According to observations, flörkeite crystallized on the vertumnite. The second sample (L2, Figure 2(b) and S1b) is less porous than L1. Esseneite, latiumite-levantite series, wollastonite, gehlenite, and garnet of the grossular-andradite-schorlomite series are the main minerals of the sample. The low-temperature mineralization is represented by flörkeite, which is grown on phillipsite-K and phillipsite-Ca (Figure 2(b)). The third sample (L3, Figure 2(c) and S1c) consists of hornfels and paralava, macroscopically nonporous. Both hornfels and paralava parts differ in grain size, but mineral associations are similar. The following minerals are associated: wollastonite, latiumite-levantite series, garnet of the grossular-andradite-schorlomite series, and gehlenite, and the accessory minerals are as follows:

TABLE 1: Chemical composition of flörkeite.

Constituent	L1			L2			L3	
	Mean ( <i>n</i> = 12)	s.d.	Range	Mean ( <i>n</i> = 6)	s.d.	Range	Mean ( <i>n</i> = 4)	s.d.
SiO <sub>2</sub>	37.39	0.52	36.57-38.46	37.10	0.39	36.42-37.63	36.07	0.50
Al <sub>2</sub> O <sub>3</sub>	31.56	0.39	31.18-32.62	31.16	0.54	30.23-31.71	30.09	0.48
CaO	8.53	0.13	8.22-8.7	8.6	0.22	8.31-8.85	8.24	0.66
SrO	n.d.			n.d.			0.39	0.3
BaO	n.d.			n.d.			1.46	0.31
Na <sub>2</sub> O	2.28	0.08	2.15-2.43	2.17	0.07	2.08-2.29	2.41	0.38
K <sub>2</sub> O	10.48	0.2	10.14-10.78	10.53	0.22	10.22-10.68	10.21	0.61
H <sub>2</sub> O	9.76			10.41			11.14	
Total	100.00			100.00			100.00	
R	0.50			0.50			0.50	
E %	3.15			1.79			-3.99	
Si	8.02			8.04			8.07	
Al	7.98			7.96			7.93	
T	16.00			16.00			16.00	
Ca	1.96			2.00			1.97	
Sr							0.05	
Ba							0.13	
Na	0.95			0.91			1.04	
K	2.87			2.91			2.91	
Extraframework	5.78			5.82			6.1	
H <sub>2</sub> O	6.98			7.52			8.31	

s.d.: standard deviation; R = Si/Al + Fe + Si; E-balance error = (Al + Fe<sup>3+</sup> - Al<sub>theor.</sub>)/Al<sub>theor.</sub> × 100Al<sub>theor.</sub> = K + Na + 2Ca + 2Sr + 2Ba [32]; water content is calculated by difference to 100%; n.d.: not detected.

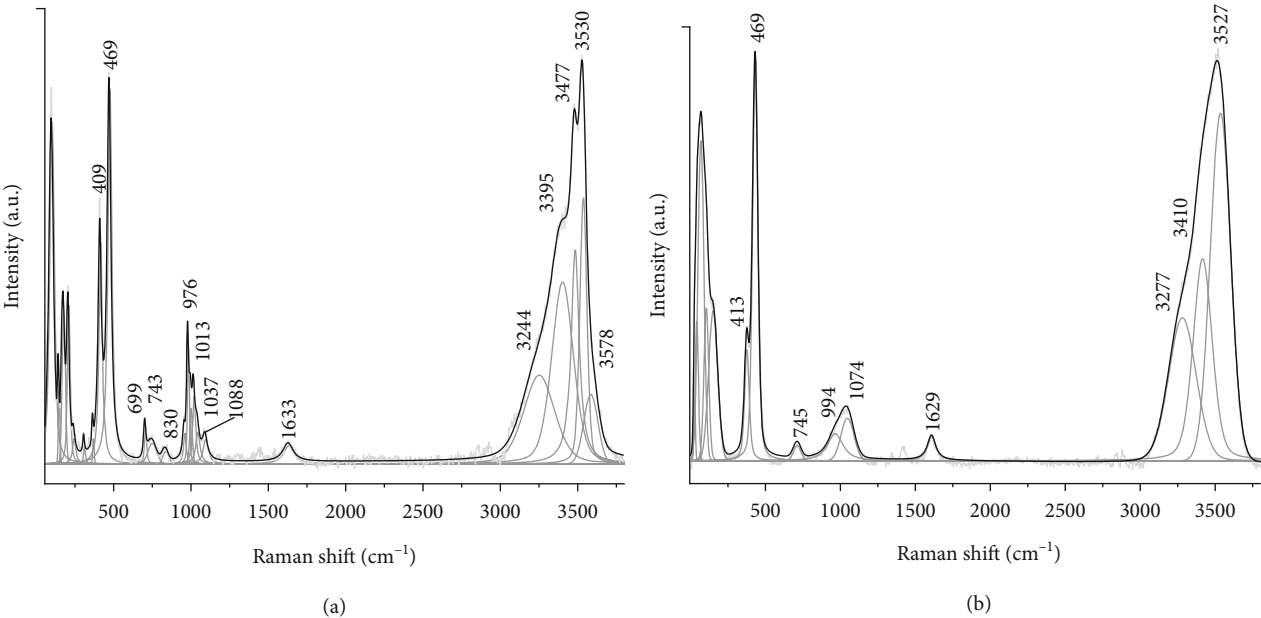


FIGURE 3: Raman spectra of (a) flörkeite and (b) phillipsite-K.

fluorapatite and perovskite (Figure S1c). In voids, zeolites such as gismondine-Ca, gismondine-Sr, thomsonite-Ca, and flörkeite occur, which usually is overgrown with gismondine-

Sr (Figure 2(c)) [28]. There is also analcime, which surrounds the voids, and minerals of the tobermorite supergroup. Baryte crystals were rarely observed. Additionally, vertumnite is



present in the low-temperature association (Figure 2(d)). Its crystals are characterized by zoning due to the increased barium content in the cores and rims. In gehlenite hornfels, flörkeite occurs as xenomorphic crystals filling the voids and rarely as automorphic crystals. In contrast to L1 and L2, zeolite mineralization of gehlenite hornfels is definitely more diverse. In all cases, minerals of the ettringite group are rarely associated with zeolites. Also, it should be emphasized that zeolites fill voids rather than veins.

### 3. Analytical Methods

**3.1. Chemical Composition.** The preliminary chemical composition of zeolites and minerals of the host rocks was examined by scanning electron microscope (Phenom XL), equipped with an EDS (energy-dispersive X-ray spectrometer) detector. Their morphology and composition inhomogeneity were observed in backscattered electron mode. The quantitative chemical analyses of the samples L1 and L2 were obtained by electron microprobe, using a CAMECA SX100 operating at 15 keV and 10 nA. For sample L1, the spot size was defocused to 10  $\mu\text{m}$ . For sample L2, beam size of 8  $\mu\text{m}$  was used. The following lines and standards were used for both samples: NaK $\alpha$  = albite, SiK $\alpha$  = diopside, AlK $\alpha$  = orthoclase, KK $\alpha$  = orthoclase, CaK $\alpha$  = diopside, SrL $\alpha$  = celestine, and BaL $\alpha$  = baryte. Sample L3 was also investigated with the CAMECA SX100 electron microprobe analyzer at 15 kV and 10 nA. The spot size was equal to 10  $\mu\text{m}$ . The lines and standards were as follows: NaK $\alpha$  = NaCl, SiK $\alpha$  = wollastonite, AlK $\alpha$  = orthoclase, KK $\alpha$  = orthoclase, CaK $\alpha$  = wollastonite, SrL $\alpha$  = celestine, and BaL $\alpha$  = baryte.

**3.2. Raman Spectroscopy.** For a complete characterization of mineral flörkeite, Raman spectroscopy was performed. Raman spectra were collected using a confocal Raman microscope WITec alpha 300R equipped with a 488 nm laser, and a CCD camera was used to obtain the spectrum. A 30  $\mu\text{m}$  optical fiber and a monochromator with a 600  $\text{mm}^{-1}$  grating were used to record the Raman spectra. The monochromator calibration was conducted using a Raman scattering line of a silicon plate (520.7  $\text{cm}^{-1}$ ). Measurement time amounted to 3 s with an accumulation of 25 scans. The spectral resolution was 3  $\text{cm}^{-1}$ . In order to refine the Raman spectrum, the spectral software package GRAMS was used.

**3.3. SC-XRD.** Single-crystal X-ray diffraction (SC-XRD) data were collected using a Rigaku Synergy-S diffractometer equipped with a dual microfocused source and a HyPix detector. The CuK $\alpha$  radiation ( $\lambda = 1.540598 \text{ \AA}$ ) was chosen due to the small size of the crystal. Data reduction and absorption correction were conducted using the software package CrysAlisPro 40.29a. The structure was solved by direct methods using SHELXS [29]. During the refinement of the structure, which was carried out using SHELXL [30], neutral atomic scattering factors were used for all atoms.

TABLE 2: Parameters for X-ray data collection and crystal structure refinement of flörkeite.

Crystal data	
Empirical formula	$\text{K}_{3.02}\text{Ca}_{1.98}\text{Na}_{0.99}\text{Al}_{8.01}\text{Si}_{8.01}\text{O}_{44.01}$
Crystal system	Triclinic
Space group	-1
	$a = 19.9366 (2)$
	$b = 14.25170 (1)$
	$c = 8.69350 (1)$
Unit cell dimensions ( $\text{\AA}$ , $^\circ$ )	$\alpha = 88.2480 (1)$
	$\beta = 125.0960 (1)$
	$\gamma = 89.6350 (1)$
Volume ( $\text{\AA}^3$ )	2019.19 (4)
Formula weight	303.34
Data collection	
Diffractometer	Synergy-S
Radiation wavelength ( $\text{\AA}$ )	1.54184
Temperature (K)	293 (2)
Absorption coefficient ( $\text{mm}^{-1}$ )	10.582
F(000)	1352
$\theta$ range for data collection ( $^\circ$ )	3.104–80.112
	$-25 \leq h \leq 25$
Index ranges	$-17 \leq k \leq 12$
	$-11 \leq l \leq 11$
Structure refinement	
Reflections collected	27274
Independent reflections	8593
Observed data ( $I > 2\sigma(I)$ )	7486
$R_1$ , wR $_2$ ( $I > 2\sigma(I)$ )	0.0341 (wR = 0.0995)
$R_1$ , wR $_2$ (for all)	0.0390 (wR = 0.1027)
GooF	1.087
$\Delta\rho_{\text{min}}$ ( $\text{e/\AA}^{-3}$ )	-0.764
$\Delta\rho_{\text{max}}$ ( $\text{e/\AA}^{-3}$ )	0.102

### 4. Results

**4.1. Chemical Composition.** The results of flörkeite chemical microanalysis are given in Table 1. The empirical crystal-chemical formulas of flörkeite were calculated based on 16 framework T-sites. The flörkeite empirical crystal-chemical formulas were determined as follows for the corresponding localities: L1,  $(\text{K}_{2.87}\text{Ca}_{1.96}\text{Na}_{0.95})[\text{Al}_{7.93}\text{Si}_{8.07}\text{O}_{31.91}]\cdot 12\text{H}_2\text{O}$ ; L2,  $(\text{K}_{2.91}\text{Ca}_{2.00}\text{Na}_{0.91})[\text{Al}_{7.96}\text{Si}_{8.04}\text{O}_{31.94}]\cdot 12\text{H}_2\text{O}$ ; and L3,  $(\text{K}_{2.91}\text{Ca}_{1.97}\text{Na}_{1.04}\text{Ba}_{0.13}\text{Sr}_{0.05})[\text{Al}_{7.93}\text{Si}_{8.07}\text{O}_{32.16}]\cdot 12\text{H}_2\text{O}$ . The water contents calculated for flörkeite on the base of microprobe analyses are underestimated (Table 1). A similar problem was noticed for the microprobe analyses of flörkeite from the type locality [8]. The theoretical determination of water content in flörkeite based on the mean refractive index and ion polarizability gives the water content about  $12\text{H}_2\text{O}$  [31]. In the empirical formulas of the studied flörkeite, we used the water content obtained by structural data. The

TABLE 3: Atom coordinates ( $x$ ,  $y$ , and  $z$ ), equivalent isotropic displacement parameters ( $U_{\text{iso}}$ ,  $\text{\AA}^2$ ), and site occupancies of flörkeite.

Site	Atom	$x$	$y$	$z$	$U_{\text{eq}}/U_{\text{iso}}$ ( $\text{\AA}^2$ )	Occupancy
K1	K	0.42274 (4)	-0.74243 (5)	0.64599 (10)	0.03247 (15)	1
K2	K	-0.06261 (5)	-0.74923 (5)	0.73279 (13)	0.04070 (18)	1
K3	K	0.41577 (4)	-0.74191 (5)	0.11511 (11)	0.03779 (17)	1
Ca1	Ca	0.19490 (3)	-0.87734 (3)	0.05342 (7)	0.01449 (11)	1
Ca2	Ca	0.21055 (3)	-0.34979 (3)	0.04392 (7)	0.01602 (11)	1
Na1	Na	0.29854 (7)	-0.13244 (8)	0.93652 (16)	0.0263 (2)	1
Si1	Si	0.07219 (4)	-0.64049 (4)	0.57303 (8)	0.00787 (12)	1
Si2	Si	0.29350 (3)	-0.14230 (4)	0.53221 (8)	0.00739 (12)	1
Si3	Si	0.46547 (3)	-0.99945 (4)	0.21715 (8)	0.00769 (12)	1
Al1	Al	0.29108 (4)	-0.35957 (4)	0.49658 (9)	0.00808 (13)	1
Si4	Si	0.20831 (3)	-0.85633 (4)	0.48076 (8)	0.00709 (12)	1
Si5	Si	0.03798 (3)	-0.00179 (4)	0.79311 (8)	0.00726 (12)	1
Si6	Si	0.37213 (3)	-0.53873 (4)	0.79003 (8)	0.00795 (12)	1
Al2	Al	0.06494 (4)	-0.86337 (4)	0.54300 (9)	0.00771 (13)	1
Si7	Si	0.43037 (4)	-0.35693 (4)	0.43460 (8)	0.00930 (12)	1
Al3	Al	0.56986 (4)	-0.86651 (4)	0.55618 (9)	0.00805 (13)	1
Al4	Al	0.21212 (4)	-0.63933 (4)	0.51376 (9)	0.00812 (13)	1
Al5	Al	0.12924 (4)	-0.02609 (4)	0.23219 (9)	0.00729 (13)	1
Al6	Al	0.37530 (4)	-0.97002 (4)	0.77592 (9)	0.00756 (13)	1
Si8	Si	0.12877 (3)	-0.46335 (4)	0.21277 (8)	0.00783 (12)	1
Al7	Al	0.02871 (4)	-0.50803 (4)	0.78793 (9)	0.00764 (13)	1
Al8	Al	0.47077 (4)	-0.49336 (4)	0.21018 (9)	0.00857 (13)	1
O1	O	0.04250 (11)	-0.74724 (11)	0.5472 (3)	0.0168 (3)	1
O2	O	0.00647 (11)	-0.58452 (12)	0.3768 (2)	0.0167 (3)	1
O3	O	0.07405 (11)	-0.59975 (12)	0.7466 (2)	0.0159 (3)	1
O4	O	0.16495 (10)	-0.63534 (13)	0.6311 (3)	0.0171 (3)	1
O5	O	0.30313 (10)	-0.25155 (11)	0.5975 (2)	0.0133 (3)	1
O6	O	0.33896 (10)	-0.12260 (12)	0.4282 (2)	0.0143 (3)	1
O7	O	0.19641 (10)	-0.11540 (11)	0.3854 (2)	0.0126 (3)	1
O8	O	0.33293 (11)	-0.08114 (11)	0.7184 (2)	0.0139 (3)	1
O9	O	0.54823 (10)	-0.04596 (12)	0.2584 (3)	0.0157 (3)	1
O10	O	0.40609 (10)	-0.95326 (11)	0.0053 (2)	0.0133 (3)	1
O11	O	0.48473 (10)	-0.91408 (11)	0.3555 (2)	0.0124 (3)	1
O12	O	0.41394 (10)	-0.07871 (11)	0.2419 (2)	0.0122 (3)	1
O13	O	0.32858 (11)	-0.44110 (12)	0.6782 (3)	0.0180 (4)	1
O14	O	0.18954 (10)	-0.37502 (11)	0.3059 (2)	0.0111 (3)	1
O15	O	0.33573 (10)	-0.35997 (12)	0.3701 (2)	0.0149 (3)	1
O16	O	0.19584 (11)	-0.74782 (11)	0.4119 (2)	0.0143 (3)	1
O17	O	0.17532 (10)	-0.91668 (11)	0.2935 (2)	0.0126 (3)	1
O18	O	0.15676 (10)	-0.88348 (12)	0.5666 (2)	0.0147 (3)	1
O19	O	0.30417 (10)	-0.88078 (12)	0.6353 (2)	0.0159 (3)	1
O20	O	-0.04171 (10)	-0.96088 (12)	0.7740 (2)	0.0138 (3)	1
O21	O	0.07841 (10)	-0.91770 (11)	0.7436 (2)	0.0114 (3)	1
O22	O	0.01839 (10)	-1.09034 (11)	0.6629 (2)	0.0139 (3)	1
O23	O	0.11108 (10)	-1.03313 (11)	0.0097 (2)	0.0119 (3)	1
O24	O	0.31592 (10)	-0.62772 (11)	0.6847 (2)	0.0129 (3)	1
O25	O	0.10799 (10)	-0.46199 (11)	1.0016 (2)	0.0118 (3)	1
O26	O	0.38865 (10)	-0.53587 (11)	0.9965 (2)	0.0126 (3)	1

TABLE 3: Continued.

Site	Atom	<i>x</i>	<i>y</i>	<i>z</i>	$U_{eq}/U_{iso}$ (Å <sup>2</sup> )	Occupancy
O28	O	0.04743 (10)	-0.44150 (12)	0.2033 (2)	0.0152 (3)	1
O29	O	0.45816 (10)	-0.55832 (12)	0.8164 (2)	0.0155 (3)	1
O30	O	0.43204 (11)	-0.40132 (12)	0.2672 (2)	0.0161 (3)	1
O31	O	0.17464 (11)	-0.56030 (12)	0.3243 (2)	0.0170 (3)	1
O32	O	0.45985 (11)	-0.24987 (11)	0.4576 (3)	0.0155 (3)	1
O33	O	0.49284 (12)	-0.41221 (12)	0.6330 (3)	0.0201 (4)	1
W1	O	0.52962 (16)	-0.7311 (2)	1.0427 (4)	0.0474 (6)	1
W2	O	0.30993 (12)	-0.30203 (14)	0.9617 (3)	0.0232 (4)	1
W3	O	0.3133 (3)	-0.6309 (2)	0.2899 (6)	0.0838 (13)	1
W4	O	0.25178 (11)	-0.96378 (14)	0.9220 (3)	0.0218 (4)	1
W5	O	0.11174 (13)	-0.74485 (14)	1.0213 (3)	0.0262 (4)	1
W6	O	0.22652 (12)	-1.18038 (13)	1.0777 (3)	0.0215 (4)	1
W7	O	0.25039 (13)	-0.74439 (15)	0.9765 (3)	0.0317 (5)	1
W8	O	0.33720 (12)	-0.88100 (15)	0.3257 (3)	0.0242 (4)	1
W9	O	0.24838 (13)	-0.49830 (15)	0.9762 (4)	0.0343 (5)	1
W10	O	0.13807 (16)	-0.3297 (2)	0.7090 (4)	0.0555 (8)	1
W11	O	0.06612 (18)	-0.26114 (18)	0.9165 (4)	0.0523 (7)	1
W12	O	0.15461 (16)	-0.14255 (19)	0.6492 (4)	0.0399 (5)	1

presence of barium and strontium distinguishes the third sample from the others. The presented data are consistent with the end member formula  $(K_3Ca_2Na)[Al_8Si_8O_{32}] \cdot 12H_2O$  and data reported for the type specimen [8].

**4.2. Raman Spectroscopy.** Raman spectra of flörkeite and phillipsite-K are presented in Figure 3. Vibrational spectra consist of three range: 150–469  $cm^{-1}$ , 699–830  $cm^{-1}$ , and 976–1088  $cm^{-1}$  [33–35]. The main characteristic band is approximately 470  $cm^{-1}$ . It corresponds to the motion of an oxygen atom in a plane perpendicular to the T–O–T bond, which means symmetric bending T–O–T vibrations [33, 34], whereas bands below 470  $cm^{-1}$  are assigned to pore opening vibrations [33, 36]. Bands within 699 – 830  $cm^{-1}$  are attributed to symmetric stretching T–O–T vibrations. Vibrations of asymmetric stretching T–O–T motions are present between 976 and 1088  $cm^{-1}$ . In the ranges 699–830  $cm^{-1}$  and 976–1088  $cm^{-1}$ , the intratetrahedral asymmetric and symmetric stretching T–O vibrations occur, respectively [33, 35, 37]. The bands between 3244 and 3578  $cm^{-1}$  correspond to the stretching vibrations of water molecules; the bending vibrations of which are present between 1629 and 1633  $cm^{-1}$  [38].

**4.3. Crystallography and Structure Description.** The crystal structure of flörkeite was refined from SC-XRD data. Table 2 reports the details of the experimental and refinement procedure. According to the data from Tables 3 and 4, Si and Al are orderly arranged at the 16 framework sites in compliance with the Löwenstein rule and previous studies [8, 39]. The mean cation-oxygen distance of aluminum tetrahedra is 1.74 Å, and the mean length of silica tetrahedra is equal to 1.62 Å (Table 4). The interatomic distances between extrafra-

mework cations and oxygen atoms within the flörkeite structure are reported in Table 5.

Flörkeite has a **PHI** framework type with an ordered distribution of Si/Al at *T*-sites and ordered arrangement of extraframework cations. The **PHI**-type structures are constituted by double-connected 4-member rings, which form double crankshaft chains (*dcc*) (Figure 4(a)) [40–42]. In the **PHI** framework type, the *dcc* resembles a corrugated ribbon and runs parallel to the *a*-axis forming 8-membered windows on the layer perpendicular to [100] [42–44]. In the **PHI**-type structure, there are two channel systems and two types of cages [6, 8, 43, 44].

The channel system parallel to [100] consists of alternately a *phi* and an *oto* units (Figure 5(a)). The channel, confined by an 8-membered window of the *phi* units, is parallel to [010] (Figure 5(b)). Thus, the *phi* unit appears at the intersection of the two channels system (Figures 4 and 5).

The dimensions of the units vary depending on the extraframework cation content (Figure 6). In flörkeite, the *oto* units are occupied by potassium and water molecules. Two types of the *oto* units can be distinguished based on the distribution of water molecules (Figures 6(a)–6(d)). In the *oto I*, the water molecule (W11) is located in the center of the 8-member ring (Figures 6(a) and 6(b)), whereas in the *oto II*, the water molecule (W1) is within the cage (Figures 6(c) and 6(d)). In phillipsite-type minerals, the *oto* units are occupied by large cations such as K and Ba [43]. Greater diversity has been observed between the two types of *phi* units (Figures 6(e)–6(h)). The *phi I* is occupied by K, Ca, and water molecules (Figures 6(e) and 6(f)). Potassium is located near the center of the 8-membered ring (Figure 6(f)), wherein phillipsite-K water molecules are present [8]. The calcium is located within the unit (Figures 6(e) and 6(f)). Water molecules (W5, W4, and W9) are located

TABLE 4: Selected interatomic distances of the framework of flörkeite structure.

Site 1	Site 2	Distance (Å)	Site 1	Site 2	Distance (Å)
Si1	O1	1.6109 (17)	Al1	O5	1.7091 (18)
Si1	O2	1.6114 (17)	Al1	O13	1.7091 (18)
Si1	O3	1.6144 (17)	Al1	O14	1.7504 (17)
Si1	O4	1.6156 (18)	Al1	O15	1.7684 (18)
Mean		1.613	Mean		1.734
Si2	O5	1.6124 (16)	Al2	O1	1.7187 (17)
Si2	O6	1.6275 (17)	Al2	O18	1.7417 (18)
Si2	O7	1.6256 (17)	Al2	O21	1.7577 (17)
Si2	O8	1.6217 (17)	Al2	O22	1.7511 (17)
Mean		1.622	Mean		1.742
Si3	O9	1.6065 (17)	Al3	O6	1.7486 (18)
Si3	O10	1.6232 (17)	Al3	O11	1.7511 (17)
Si3	O11	1.6243 (17)	Al3	O12	1.7479 (17)
Si3	O12	1.6224 (17)	Al3	O32	1.7349 (17)
Mean		1.619	Mean		1.746
Si4	O16	1.6059 (17)	Al4	O4	1.7421 (18)
Si4	O17	1.6385 (17)	Al4	O16	1.7432 (17)
Si4	O18	1.6224 (17)	Al4	O24	1.7324 (17)
Si4	O19	1.6091 (17)	Al4	O31	1.7322 (18)
Mean		1.619	Mean		1.737
Si5	O20	1.6030 (17)	Al5	O7	1.7352 (17)
Si5	O21	1.6281 (16)	Al5	O17	1.7508 (17)
Si5	O22	1.6159 (17)	Al5	O20	1.7263 (17)
Si5	O23	1.6292 (16)	Al5	O23	1.7573 (17)
Mean		1.619	Mean		1.742
Si6	O13	1.6020 (17)	Al6	O8	1.7469 (17)
Si6	O24	1.6162 (17)	Al6	O9	1.7288 (18)
Si6	O26	1.6297 (17)	Al6	O10	1.7421 (17)
Si6	O29	1.6157 (17)	Al6	O19	1.7354 (17)
Mean		1.616	Mean		1.738
Si7	O15	1.6317 (17)	Al7	O2	1.7321 (17)
Si7	O30	1.6222 (18)	Al7	O3	1.7440 (17)
Si7	O32	1.6150 (17)	Al7	O25	1.7581 (17)
Si7	O33	1.6063 (18)	Al7	O28	1.7237 (18)
Mean		1.619	Mean		1.739
Si8	O14	1.6316 (16)	Al8	O26	1.7559 (18)
Si8	O25	1.6325 (17)	Al8	O29	1.7269 (18)
Si8	O28	1.6037 (17)	Al8	O30	1.7404 (17)
Si8	O31	1.6025 (17)	Al8	O33	1.7131 (18)
Mean		1.618	Mean		1.734
Total mean		1.618	Total mean		1.739

TABLE 5: Selected interatomic distances of the extraframework cations in flörkeite structure.

Site 1	Site 2	Distance (Å)	Site 1	Site 2	Distance (Å)
K1	W1	2.837 (3)	Ca2	O14	2.5574 (17)
K1	O24	2.8521 (18)	Ca2	O15	2.4744 (18)
K1	O29	2.9387 (18)	Ca2	O25	2.4668 (17)
K1	O32	2.9547 (19)	Ca2	W2	2.553 (2)
K1	W3	2.959 (4)	Ca2	W6	2.4418 (19)
K1	O19	3.0499 (18)	Ca2	W9	2.442 (2)
K1	O9	3.0647 (18)	Ca2	W10	2.399 (3)
K1	W8	3.079 (2)	Ca2	W11	2.705 (3)
K2	O28	2.7746 (18)	Na	O8	2.453 (2)
K2	W5	2.892 (2)	Na	O12	2.460 (2)
K2	O14	2.9292 (17)	Na	W12	2.506 (3)
K2	O7	2.9881 (18)	W1	K3	2.686 (3)
K2	O20	3.0243 (18)	W2	Ca2	2.553 (2)
K2	W11	3.098	W4	Ca1	2.3804 (19)
K2	W12	3.180 (3)	W5	Ca1	2.406 (2)
K2	O1	3.298 (2)	W6	Ca2	2.4418 (19)
K2	W10	3.369 (3)	W7	K3	2.786 (2)
K3	W1	2.686 (3)	W9	Ca2	2.443 (2)
K3	W7	2.786 (2)	W10	K2	3.369 (3)
K3	O11	2.9355 (18)	W11	K2	3.098 (4)
K3	O33	2.949 (2)	W12	K2	3.180 (3)
K3	O26	3.0218 (18)	W4	Na	2.546 (2)
K3	O32	3.056 (2)	W6	Na	2.5454 (2)
K3	O10	3.1610 (18)	W7	Ca1	2.462 (2)
K3	O24	3.4106 (18)	W9	Ca2	2.442 (2)
Ca1	O17	2.3854 (17)	W10	Ca2	2.399
Ca1	O21	2.4283 (17)	W11	Ca2	2.705 (3)
Ca1	O23	2.6899 (17)			
Ca1	W4	2.3803 (19)			
Ca1	W5	2.406 (2)			
Ca1	W7	2.462 (2)			
Ca1	W8	2.434 (2)			

near the center of the 8-membered rings, which build the unit. W8 and W3 water molecules are found in a cavity formed by a double crankshaft chain (Figures 6(e) and 6(f)). The *phi II* unit is closer to the phillipsite-K structure

[6, 8, 43]. Na and Ca cations and water molecules are inside the *phi II* unit [6, 43, 44]. However, in phillipsite-K, the Na position is equivalent to the Ca site, and the Ca site is a counterpart of the water position [8]. The symmetry of the **PHI** structure aristotype (topological symmetry) is *Cmcm*, which is reduced to *P2<sub>1</sub>/m* [8, 40, 41, 45] as a result of a slight distortion induced on the tetrahedral framework by the presence of larger cations (K and Ba) [7]. Full occupancy of large cations position in flörkeite structure increased the distortion of the framework. The topochemical symmetry of flörkeite is lowered to *B2/b* due to ordered Si/Al distribution in the tetrahedral framework, which is the main difference between flörkeite and phillipsite minerals [8, 40]. As noted by Lengauer et al. [8], the atomic coordinates of the framework do not exhibit significant differences in the two minerals (Table 3). A comparison of the unit cell parameters of phillipsite and flörkeite



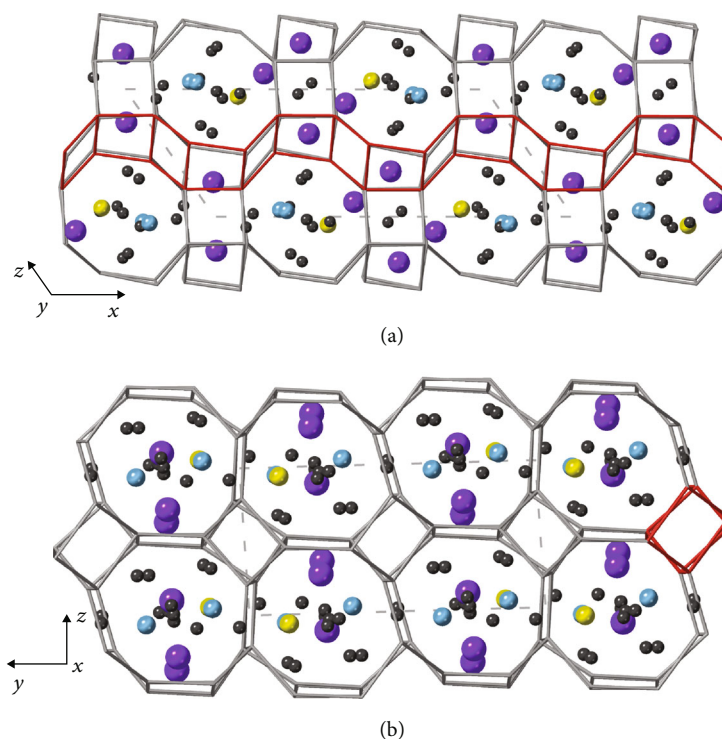


FIGURE 4: Extraframework cations in flörkeite framework: (a) projection along  $[010]$ ; (b) projection of framework with extraframework cations along  $[100]$ , a double crankshaft chain is marked red. Potassium, calcium, and sodium are purple, blue, and yellow spheres, respectively. Dark grey spheres represent  $\text{H}_2\text{O}$  sites.

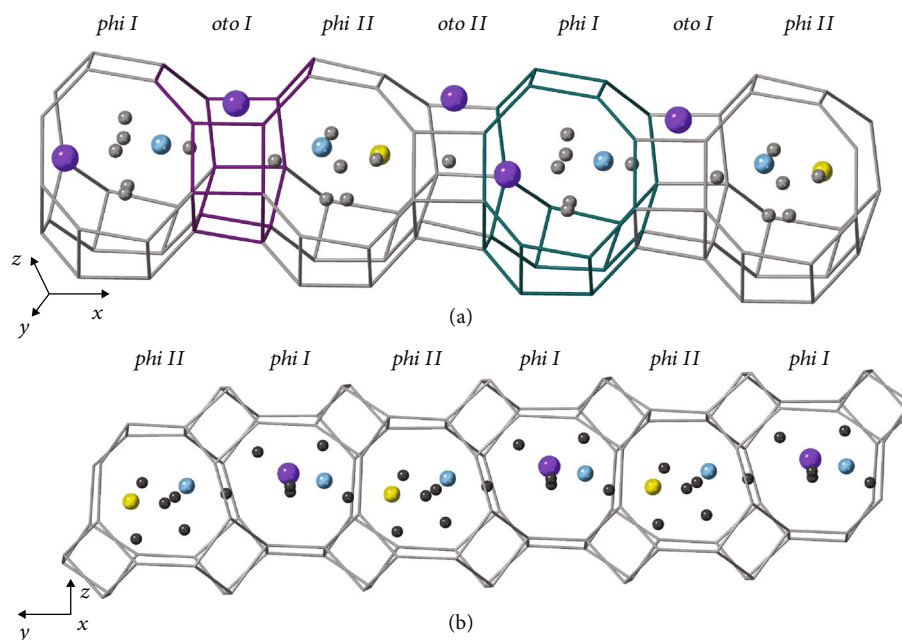


FIGURE 5: (a) Channel running along  $[100]$  within flörkeite structure: the *phi* unit is marked by green color, and the *oto* unit is marked by purple color; (b) channel composed of *phi* units running along  $[010]$  in flörkeite structure. Potassium, calcium, and sodium are purple, blue, and yellow spheres, respectively. Dark grey spheres represent  $\text{H}_2\text{O}$  sites.

revealed the doubling of  $a$  parameter in flörkeite, which is a consequence of the ordered arrangement of extraframework cations (Figure 5(a), [8]). The ordered distribution of extra-

framework cations within flörkeite channels causes a reduction of the topochemical symmetry to the triclinic real symmetry [8].

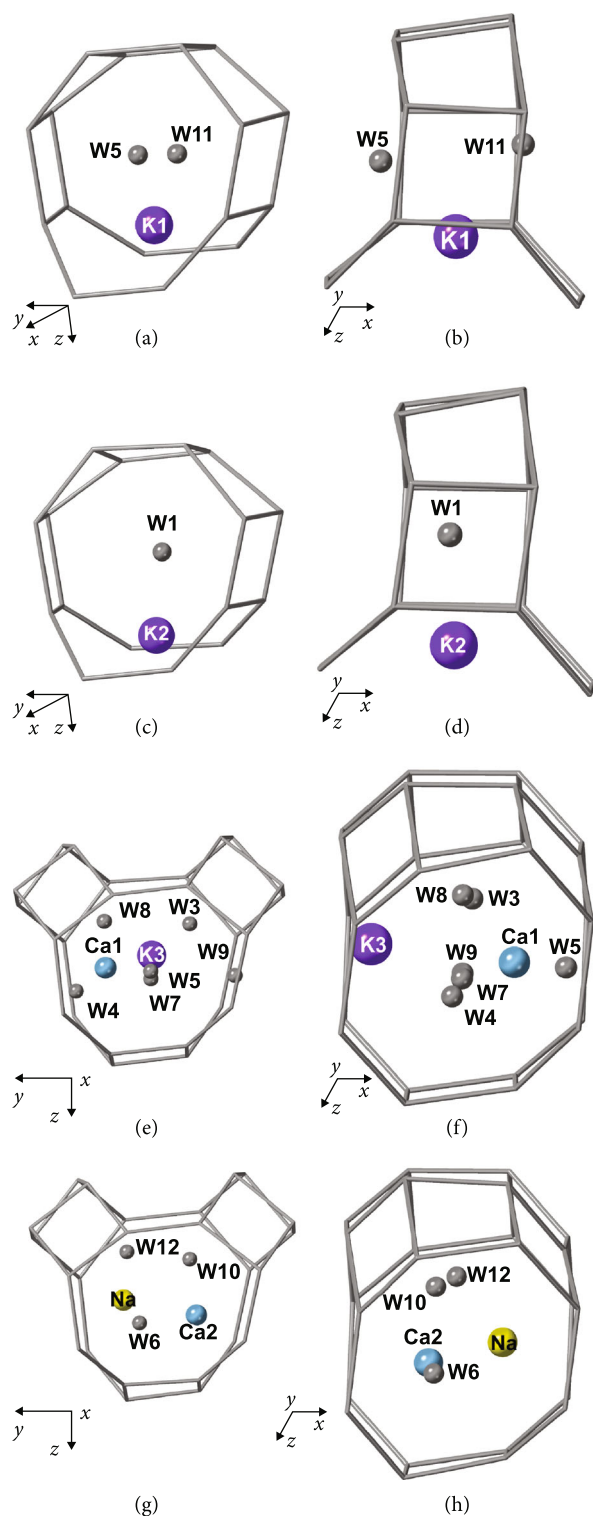


FIGURE 6: (a, b) The *oto I* unit in two orientations occupied by potassium (K1), the water molecule at W11 is near the center of the 8-membered ring; (c, d) the *oto II* unit is filled by potassium (K2) and a water molecule at W1; (e, f) the *phi I* in two orientations occupied by calcium (Ca1) and potassium (K3), which is located near the center of 8-membered ring, and water molecules: W3, W4, W5, W7, W8, and W9; (g, h) the *phi II* in two orientations, which is occupied by calcium (Ca2), sodium (Na), and water molecules W6, W10, and W12.

## 5. Discussion

The Hatrurim Complex is the second occurrence of flörkeite, which is the most abundant zeolite in the voids of high-temperature pyrometamorphic rocks. The obtained results on flörkeite from the Hatrurim Complex are similar to those on the type flörkeite from the Bellerberg volcano. The structure of the studied flörkeite does not differ significantly from the crystal structure of the type specimen ( $(K_{2.96}, Ca_{2.04}, Na_{1.02}, Mg_{0.01})[Al_{8.03}Si_{7.97}O_{31.97}] \cdot 11.72H_2O$ ;  $a = 19.965(1) \text{ \AA}$ ,  $b = 14.274(1) \text{ \AA}$ ,  $c = 8.704(1) \text{ \AA}$ ,  $\alpha = 88.37(1)^\circ$ ,  $\beta = 125.08(1)^\circ$ ,  $\gamma = 89.57(1)^\circ$ , and  $V = 2028.2(3) \text{ \AA}^3$ ; [8]). Also, the empirical formulas of flörkeite from the three localities of the Hatrurim Basin are close to the ideal formula (Table 1, [8]). The flörkeite and phillipsite-K Raman spectra show strong similarities (Figure 3), indicating that the main band at  $\sim 470 \text{ cm}^{-1}$ , characteristics of the **PHI**-type structures, does not depend on the framework ordering and Si/Al ratio. The symmetric and asymmetric stretching T-O-T vibration in the region  $700\text{--}1100 \text{ cm}^{-1}$  of flörkeite spectrum confirms its ordered framework. The wide complex band of water molecule vibrations in the phillipsite-K spectrum indicates a disordered arrangement of partially occupied sites by water. Overall, the general features of the spectra are unchanged, and the Si/Al ordering at the tetrahedral sites induces minor differences. The chemical composition of L1 and L2 samples does not show significant differences. In the L1 sample of amygdaloidal paralava, flörkeite occurs in voids and associates with vertumnite ( $Ca_4Al_4Si_4O_6(OH)_{24} \cdot 3H_2O$ ), in which no barium impurity was revealed. The chemical composition of zeolites from the latiumite-esseneite rock is relatively homogenous. Comparing phillipsite series  $K_2(Ca_{0.5}Na)_4(Al_6Si_{10})O_{32} \cdot 12H_2O$  and flörkeite  $(K_3Ca_2Na)[Al_8Si_8O_{32}] \cdot 12H_2O$  formulas reveals the depletion of extraframework cations in phillipsite minerals, balanced by the higher Si/Al ratio. Overgrowing flörkeite on phillipsite-K indicates a decrease of the Si/Al and Ca/(K + Na) ratio (Figure 2). A little amount of strontium and barium impurities distinguish the flörkeite composition of sample L3 (Table 1). In the **PHI**-type structures, barium substitutes potassium in the *oto* units [43]. In contrast, according to ion-exchanged phillipsite data, strontium could be present in *oto* and *phi* units [44]. Among the analyzed pyrometamorphic rock samples, gehlenite hornfels is distinguished by the greatest variety of zeolite mineralization. Likewise to the Bellerberg volcano, apart from flörkeite, other high-aluminum zeolites, such as gismondine-Sr, gismondine-Ca, and thomsonite-Ca, have been reported [28]. The presented data on flörkeite in voids of gehlenite hornfels and the presence of gismondine-Sr and Ba-bearing vertumnite (Table 1) point out the high content of barium and strontium in the low-temperature mineralization of these rocks. The sharp boundary between Ba-rich and Ba-poor vertumnite indicates an intense increase in the barium content in the crystallization medium (Figure 2). Moreover, gehlenite hornfels enrichment in barium and strontium is in agreement with the previous studies [22, 23, 46]. These elements have been dispersed in the baryte-hashemite and fluorapatite-fluorellestadite series [23,

47]. Zeolite mineralization of pyrometamorphic rocks varies compared to zeolite-bearing olive unit rocks. In zeolite-bearing rocks of the olive unit, zeolites such as thomsonite-Ca and gismondine-Ca are predominant. Phillipsite-Ca and clinoptilolite-Ca are rarely observed. Compared to the present data, the zeolite mineralization of the olive unit is characterized by a higher Si/Al ratio, as evidenced by the presence of clinoptilolite  $\text{Ca}_3(\text{Si}_{30}\text{Al}_6)\text{O}_{72}\cdot 20\text{H}_2\text{O}$ . Si/Al ratio differences could be related to the protoliths diversity [48–50]. A low Si/Al ratio in zeolites displays a highly alkaline environment [1, 48, 50–53]. The favourable pH for zeolite crystallization is around 9–10 [1, 48, 54]. The crystallization sequence of the low-temperature mineralization in all samples corresponds to the  $\text{Ca}/(\text{K}+\text{Na})$  ratio decrease. Thus, the formation process of zeolite mineralization could be divided into two steps: the first step was characterized by the higher calcium content, whereas monovalent cations were dominant in the second step. As a result, flörkeite is formed at the end of a low-temperature crystallization sequence (Figure 2).

## 6. Conclusions

Zeolite flörkeite, known only from the xenolith in the Bellerberg volcano area, Germany, is a widespread low-temperature mineral in voids of gehlenite-bearing pyrometamorphic rocks in the Hatrurim Complex, Israel. It is a fully ordered zeolite characterized by the highest aluminium content among phillipsite-type zeolites. For the first time, Raman spectrum of flörkeite has been collected. The Raman spectroscopy investigation of PHI-type minerals indicates that the position of the main band at  $470\text{ cm}^{-1}$  does not depend on the Si/Al ratio and ordering at tetrahedral sites. Zeolitization in pyrometamorphic rocks of the Hatrurim Basin features a low silica activity and high pH conditions resulting from the reaction between meteoric waters and clinker-like rocks [55]. The zeolite mineralization of amygdale results from meteoric water circulations in pyrometamorphic rocks during their cooling [4, 9, 56, 57]. Extremely high aluminum contents are caused by the alteration of rock-forming minerals such as gehlenite, mayenite group minerals, ye'elimite, levantite-latiumite series, and kalsilite. The occurrence of flörkeite in different pyrometamorphic rocks indicates the relatively uniform, regional forming conditions, and open hydrologic system of zeolitization.

## Data Availability

All data generated or analyzed during this study are included in this published article and its supplementary materials. Primary data are available from the corresponding author on request.

## Conflicts of Interest

The authors declare that they have no conflicts of interest.

## Acknowledgments

Investigations were supported by the National Science Center of Poland Grant (grant number UMO-2019/35/O/ST10/01015) and Preludium Bis 1 Project of the Polish National Agency for Academic Exchange. The Swiss National Science Foundation (SNF) is acknowledged for the R'Equip (grant number 206021\_177033).

## Supplementary Materials

Figure 1S: general view of rock-forming minerals in (a) the L1 sample amygdaloidal paralava and (b) the L2 sample esseneite-latiumite paralava; (c) the L3 sample, boundary between fine-grained hornfels and coarse-grained paralava is visible. Adr: andradite; Chr: chromite; Cls: celsian; Ess: esseneite; Fap: fluorapatite; Gh: gehlenite; Grs: grossular; Kls: kalsilite; Lat: latiumite; Wo: wollastonite. (*Supplementary Materials*)

## References

- [1] R. L. Hay and R. A. Sheppard, "Occurrence of zeolites in sedimentary rocks: an overview," *Reviews in Mineralogy and Geochemistry*, vol. 45, pp. 217–232, 2001.
- [2] M. Utada, "Zeolites in hydrothermally altered rocks," *Reviews in Mineralogy and Geochemistry*, vol. 45, no. 1, pp. 305–322, 2001.
- [3] F. Bernhard and U. Barth-Wirsching, "Zeolitization of a phonolitic ash flow by groundwater in the Laach volcanic area, Eifel, Germany," *Clays and Clay Minerals*, vol. 50, no. 6, pp. 710–725, 2002.
- [4] T. B. Weisenberger, S. Spürgin, and Y. Lahaye, "Hydrothermal alteration and zeolitization of the Fohberg phonolite, Kaiserstuhl volcanic complex, Germany," *International Journal of Earth Sciences*, vol. 103, no. 8, pp. 2273–2300, 2014.
- [5] R. A. Sheppard and R. L. Hay, "Formation of zeolites in open hydrologic systems," *Reviews in Mineralogy and Geochemistry*, vol. 45, pp. 261–273, 2001.
- [6] G. D. Gatta, P. Cappelletti, N. Rotiroli, C. Slebodnick, and R. Rinaldi, "New insights into the crystal structure and crystal chemistry of the zeolite phillipsite," *American Mineralogist*, vol. 94, no. 1, pp. 190–199, 2009.
- [7] E. Passaglia and A. Sheppard, "The Crystal Chemistry of Zeolites," *Reviews in Mineralogy and Geochemistry*, vol. 45, pp. 69–116, 2001.
- [8] C. L. Lengauer, U. Kolitsch, and E. Tillmanns, "Flörkeite,  $\text{K}_3\text{Ca}_2\text{Na}[\text{Al}_8\text{Si}_8\text{O}_{32}]\cdot 12\text{H}_2\text{O}$ , a new phillipsite-type zeolite from the Bellerberg, East Eifel volcanic area, Germany," *European Journal of Mineralogy*, vol. 21, no. 4, pp. 901–913, 2009.
- [9] Ł. Kruszewski, V. Palchik, Y. Vapnik, K. Nowak, K. Banasik, and I. Galuskina, "Mineralogical, geochemical, and rock mechanic characteristics of zeolite-bearing rocks of the Hatrurim basin, Israel," *Minerals*, vol. 11, no. 10, p. 1062, 2021.
- [10] Y. K. Bendor, "Israel," *Lexique Stratigraphique International, Asie*, vol. III, p. 80, 1960.
- [11] S. Gross, "The mineralogy of the Hatrurim formation, Israel," *Geological Survey of Israel Bulletin*, vol. 70, 1977.
- [12] A. Burg, A. Starinsky, Y. Bartov, and Y. Kolodny, "Geology of the Hatrurim formation ("Mottled Zone") in the Hatrurim



- basin," *Israel Journal of Earth Sciences*, vol. 40, pp. 107–124, 1991.
- [13] A. Burg, Y. Kolodny, and V. Lyakhovsky, "Hatrurim-2000: the "Mottled Zone" revisited, forty years later," *Israel Journal of Earth Sciences*, vol. 48, pp. 209–223, 1999.
  - [14] Y. V. Seryotkin, E. V. Sokol, S. N. Kokh, and V. V. Sharygin, "Natural bentorite— $\text{Cr}^{3+}$  derivate of ettringite: determination of crystal structure," *Phys Chem Minerals*, vol. 46, no. 6, pp. 553–570, 2019.
  - [15] I. Novikov, Y. Vapnik, and I. Safonova, "Mud volcano origin of the Mottled Zone, south Levant," *Geoscience Frontiers*, vol. 4, no. 5, pp. 597–619, 2013.
  - [16] I. O. Galuskina, Y. Vapnik, B. Lazic, T. Armbruster, M. Murashko, and E. V. Galuskin, "Harmunite  $\text{CaFe}_2\text{O}_4$ : a new mineral from the Jabal Harmun, West Bank, Palestinian Autonomy, Israel," *American Mineralogist*, vol. 99, no. 5-6, pp. 965–975, 2014.
  - [17] E. V. Sokol, I. S. Novikov, S. N. Zateeva, V. V. Sharygin, and Y. E. Vapnik, "Pyrometamorphic rocks of the spurritermerwinite facies as indicators of hydrocarbon discharge zones (the Hatrurim formation, Israel)," *Doklady Earth Sciences*, vol. 420, no. 1, pp. 608–614, 2008.
  - [18] E. Sokol, I. Novikov, S. Zateeva, Y. E. Vapnik, R. Shagam, and O. Kozmenko, "Combustion metamorphism in the Nabi Musa dome: new implications for a mud volcanic origin of the Mottled Zone, Dead Sea area," *Basin Research*, vol. 22, no. 4, pp. 414–438, 2010.
  - [19] Y. Kolodny, M. Bar, and E. Sass, "Fission track age of the Mottled Zone event' in Israel," *Earth and Planetary Science Letters*, vol. 11, no. 1-5, pp. 269–272, 1971.
  - [20] Y. Kolodny, A. Burg, Y. I. Geller, L. Halicz, and Y. Zakon, "Veins in the combusted metamorphic rocks, Israel; weathering or a retrograde event?," *Chemical Geology*, vol. 385, pp. 140–155, 2014.
  - [21] D. Gur, G. Steinitz, Y. Kolodny, A. Starinsky, and M. McWilliams, "40Ar/39Ar dating of combustion metamorphism ("Mottled Zone", Israel)," *Chemical Geology*, vol. 122, no. 1-4, pp. 171–184, 1995.
  - [22] E. V. Sokol, S. N. Kokh, Y. Vapnik, V. Thiery, and S. A. Korzhova, "Natural analogs of belite sulfoaluminate cement clinkers from Negev desert, Israel," *American Mineralogist*, vol. 99, no. 7, pp. 1471–1487, 2014.
  - [23] E. Sokol, S. Kokh, V. Sharygin et al., "Mineralogical diversity of  $\text{Ca}_2\text{SiO}_4$ -bearing combustion metamorphic rocks in the Hatrurim basin: implications for storage and partitioning of elements in oil shale clinkering," *Minerals*, vol. 9, no. 8, p. 465, 2019.
  - [24] E. V. Galuskin, B. Krüger, I. O. Galuskina et al., "Levantite,  $\text{KCa}_3(\text{Al}_2\text{Si}_3\text{O}_{11}(\text{PO}_4))$ , a new latiumite-group mineral from the pyrometamorphic rocks of the Hatrurim basin, Negev desert, Israel," *Mineralogical Magazine*, vol. 83, no. 5, pp. 713–721, 2019.
  - [25] E. V. Sokol, O. L. Gaskova, S. N. Kokh et al., "Chromatite and its  $\text{Cr}^{3+}$ - and  $\text{Cr}^{6+}$ -bearing precursor minerals from the Nabi Musa Mottled Zone complex, Judean Desert," *American Mineralogist*, vol. 96, no. 4, pp. 659–674, 2011.
  - [26] R. Juroszek, B. Krüger, I. Galuskina, H. Krüger, Y. Vapnik, and E. Galuskin, "Siwagaite,  $\text{Ca}_6\text{Al}_2(\text{CrO}_4)_3(\text{OH})_{12}\cdot 26\text{H}_2\text{O}$ , a new mineral of the ettringite group from the pyrometamorphic Daba-Siwaga complex, Jordan," *American Mineralogist*, vol. 105, no. 3, pp. 409–421, 2020.
  - [27] F. Hirsch, A. Burg, and Y. Avani, "Geological map of Israel 1:50 000 arade sheet," *Geological Survey*, 2008.
  - [28] K. Nowak, G. Cametti, I. O. Galuskina, Y. Vapnik, and E. V. Galuskin, "Gismondine-Sr,  $\text{Sr}_4(\text{Al}_3\text{Si}_8\text{O}_{32})\cdot 9\text{H}_2\text{O}$ , a new strontium dominant, orthorhombic zeolite of the gismondine series from the Hatrurim Complex, Israel," *American Mineralogist*, 2022.
  - [29] G. M. Sheldrick, "A short history of SHELX," *Acta Crystallographica Section A: Foundations of Crystallography*, vol. 64, no. 1, pp. 112–122, 2008.
  - [30] G. M. Sheldrick, "Crystal structure refinement with SHELXL," *Structural Chemistry*, vol. 71, Part 1, pp. 3–8, 2015.
  - [31] R. X. Fischer, M. Burianek, and R. D. Shannon, "Determination of the  $\text{H}_2\text{O}$  content in minerals, especially zeolites, from their refractive indices based on mean electronic polarizabilities of cations," *European Journal of Mineralogy*, vol. 32, no. 1, pp. 27–40, 2020.
  - [32] E. Passaglia, "The crystal chemistry of chabazites," *American Mineralogist*, vol. 55, no. 7-8, pp. 1278–1301, 1970.
  - [33] S. M. Auerbach, K. A. Carrado, and P. K. Dutta, *Handbook of Zeolite Science and Technology*, M. Dekker, New York, 2003.
  - [34] J. Čejka, *Introduction to Zeolite Science and Practice*, Elsevier, Amsterdam; Boston, 3rd rev. ed. edition, 2007.
  - [35] A. W. Chester and E. G. Derouane, *Zeolite Chemistry and Catalysis*, Springer Netherlands, Dordrecht, 2009.
  - [36] W. Mozgawa, "The relation between structure and vibrational spectra of natural zeolites," *Journal of Molecular Structure*, vol. 596, no. 1-3, pp. 129–137, 2001.
  - [37] A. C. Gujar, A. A. Moye, P. A. Coghill, D. C. Teeters, K. P. Roberts, and G. L. Price, "Raman investigation of the SUZ-4 zeolite," *Microporous and Mesoporous Materials*, vol. 78, no. 2-3, pp. 131–137, 2005.
  - [38] Y.-L. Tsai, E. Huang, Y. H. Li et al., "Raman spectroscopic characteristics of zeolite group minerals," *Minerals*, vol. 11, no. 2, p. 167, 2021.
  - [39] W. Loewenstein, "The distribution of aluminum in the tetrahedra of silicates and aluminates," *American Mineralogist*, vol. 39, no. 1–2, pp. 92–96, 1954.
  - [40] G. Gottardi, "Topologic symmetry and real symmetry in framework silicates," *Mineralogy and Petrology*, vol. 26, no. 1-2, pp. 39–50, 1979.
  - [41] G. Gottardi and E. Galli, *Natural zeolites*, Springer Science & Business Media, 1985.
  - [42] T. Armbruster and E. Gunter, "Crystal structures of natural zeolites," *Reviews in Mineralogy and Geochemistry*, vol. 45, pp. 1–68, 2001.
  - [43] R. Rinaldi, J. J. Pluth, and J. V. Smith, "Zeolites of the phillipsite family. Refinement of the crystal structures of phillipsite and harmotome," *Acta Crystallographica - Section B: Structural Crystallography & Crystal Chemistry*, vol. 30, no. 10, pp. 2426–2433, 1974.
  - [44] A. F. Gualtieri, E. Passaglia, E. Galli, and A. Viani, "Rietveld structure refinement of Sr-exchanged phillipsites," *Microporous and Mesoporous Materials*, vol. 31, no. 1–2, pp. 33–43, 1999.
  - [45] G. D. Gatta and Y. Lee, "Anisotropic elastic behaviour and structural evolution of zeolite phillipsite at high pressure: a synchrotron powder diffraction study," *Microporous and Mesoporous Materials*, vol. 105, no. 3, pp. 239–250, 2007.



- [46] Y. I. Geller, A. Burg, L. Halicz, and Y. Kolodny, "System closure during the combustion metamorphic "Mottled Zone" event, Israel," *Chemical Geology*, vol. 334, pp. 25–36, 2012.
- [47] R. Juroszek, B. Krüger, K. Banasik, Y. Vapnik, and I. Galuskina, "Raman spectroscopy and structural study of baryte-hashemite solid solution from pyrometamorphic rocks of the Hatrurim Complex, Israel," *Spectrochimica Acta Part A: Molecular and Biomolecular Spectroscopy*, vol. 205, pp. 582–592, 2018.
- [48] A. Langella, P. Cappelletti, and M. de' Gennaro, "Zeolites in closed hydrologic systems," *Reviews in Mineralogy and Geochemistry*, vol. 45, pp. 235–257, 2001.
- [49] J. M. R. Trian, R. J. F. Herrera, R. C. A. Rios et al., "Natural zeolites filling amygdals and veins in basalts from the British Tertiary Igneous Province on the Isle of Skye, Scotland," *Earth Sciences Research Journal*, vol. 16, no. 1, pp. 41–53, 2012.
- [50] D. Novembre, D. Gimeno, P. Cappelletti, and S. F. Graziano, "A case study of zeolitization process: "Tufo Rosso a Scorie Nere" (Vico volcano, Italy): inferences for a general model," *European Journal of Mineralogy*, vol. 33, no. 3, pp. 315–328, 2021.
- [51] R. H. Mariner and R. C. Surdam, "Alkalinity and formation of zeolites in saline alkaline lakes," *Science*, vol. 170, no. 3961, pp. 977–980, 1970.
- [52] E. Passaglia, G. Vezzadini, and R. Carnevali, "Diagenetic chabazites and phillipsites in Italy: crystal chemistry and genesis," *European Journal of Mineralogy*, vol. 2, no. 6, pp. 827–840, 1990.
- [53] S. J. Chipera and J. A. Apps, "Geochemical Stability of Natural Zeolites," *Reviews in Mineralogy and Geochemistry*, vol. 45, pp. 117–157, 2001.
- [54] M. Kousehlar, T. B. Weisenberger, F. Tutti, and H. Mirnejad, "Fluid control on low-temperature mineral formation in volcanic rocks of Kahrizak, Iran," *Geofluids*, vol. 12, no. 4, p. 311, 2012.
- [55] A. E. Milodowski, L. Trotignon, H. Khoury et al., "The Analogue Cement ZOne (ACZ)," in *a Natural Analog Study of Cement Buffered, Hyperalkaline Groundwaters and their Interaction with a Repository Host Rock IV: An Examination of the Khushaym Matruk (Central Jordan) and Maqarin (Northern Jordan) Sites, Chapter 4*, NDA, Moors Row, U.K, 2011.
- [56] S. Spürigin, T. B. Weisenberger, and M. Marković, "Zeolite-group minerals in phonolite-hosted deposits of the Kaiserstuhl volcanic complex, Germany," *American Mineralogist*, vol. 104, no. 5, pp. 659–670, 2019.
- [57] P. C. Piilonen, G. Poirier, W. Lechner, R. Rowe, and R. P. Richards, "Zeolite minerals from Wat Ocheng, Ta Ang, Ratanakiri Province, Cambodia – occurrence, composition, and paragenesis," *The Canadian Mineralogist*, vol. 60, no. 1, pp. 133–153, 2022.